The Astrophysical Journal, 993:219 (9pp), 2025 November 10 https://doi.org/10.3847/1538-4357/ae12a1

Slab Turbulence in the Very Local Interstellar Medium and the IBEX Ribbon

E. J. Zirnstein[1], D. J. McComas[1], J. Giacalone[2], G. P. Zank[3], F. Guo[4], J. Heerikhuisen[5], H. Li[4], and D. B. Reisenfeld[4]
[1] Department of Astrophysical Sciences, Princeton University, Princeton, NJ 08544, USA; ejz@princeton.edu
[2] Lunar and Planetary Laboratory, University of Arizona, Tucson, AZ 85721, USA
[3] Department of Space Sciences, The University of Alabama in Huntsville, Huntsville, AL 35805, USA
[4] Intelligence and Space Research, Los Alamos National Laboratory, Los Alamos, NM 87545, USA
[5] Department of Mathematics and Statistics, University of Waikato, Hamilton, New Zealand
Received 2025 July 30; revised 2025 September 29; accepted 2025 October 10; published 2025 November 6

Abstract

In this study, we analyze an important property of the very local interstellar medium, i.e., turbulence that affects the intensity and shape of the Interstellar Boundary Explorer (IBEX) ribbon. Specifically, we simulate the propagation of the ribbon's parent ions before they become secondary energetic neutral atoms that can be observed at 1 au by IBEX. We then test how different slab/2D turbulence fractions affect the intensity and shape of the modeled ribbon and compare to the latest IBEX ribbon-separated data. We compare 1D cuts across the modeled and observed ribbon as a function of angle away from the ribbon center. We find that the intensities of the modeled ribbon are larger than most of the data, except near the ecliptic plane. However, the model intensities are sensitive to how we model the neutral solar wind, which forms the source ion population for the ribbon. We then compare the model and data by normalizing the fluxes to their respective peak intensities and find the peaks' angular distances from the ribbon center. We find that most of the model peaks lie within 3° of the data peaks, which we consider our 1σ uncertainty (half the size of an IBEX pixel). By averaging the instances where the model peaks match the data peaks (within 3°), we find that the mean is slab-50%, with a standard deviation of ±28% and standard error of ±5%.

Unified Astronomy Thesaurus concepts: Heliosphere (711); Solar wind (1534); Interstellar magnetic fields (845); Pickup ions (1239); Ion-neutral reactions (2263); Interstellar medium (847)

1. Introduction

A nonthermal distribution of pickup ions (PUIs) is produced in the solar wind (SW) by the ionization of interstellar neutrals that enter our heliosphere. As PUIs are generated in the supersonic SW, the subsequently neutralized SW protons (energetic neutral atoms; ENAs) travel radially outward, with a mean free path similar to the size of the heliosphere due to the low plasma density. However, outside the heliopause, the very local interstellar medium (VLISM) plasma density is ∼50 times larger than the heliosheath plasma density (D. A. Gurnett et al. 2013; D. A. Gurnett & W. S. Kurth 2019). This reduces the mean free path of ENAs traveling through the VLISM by a similar factor, such that some will experience charge exchange with interstellar protons. The source distribution stretches from the heliopause to a few hundred astronomical units beyond the heliopause in the draped interstellar magnetic field (ISMF; E. J. Zirnstein et al. 2015, 2016). These newly generated PUIs from the neutral SW (PINS; E. J. Zirnstein et al. 2019) gyrate around the local ISMF until another charge exchange event occurs. The majority of 1.1 keV PINS (∼63%), for example, will charge exchange within ∼2 yr, assuming a neutral H density of $\sim 0.2\,\mathrm{cm}^{-3}$. After charge exchange, some of these "secondary ENAs" can travel back into the heliosphere, and a tiny fraction are detected by the Interstellar Boundary Explorer (IBEX; D. J. McComas et al. 2009a, 2009b; J. Heerikhuisen et al. 2010) from lines of sight ($\boldsymbol{r}$) nearly perpendicular to the draped, local ISMF ($\boldsymbol{B}_{\mathrm{VLISM}}$), i.e., $\boldsymbol{B}_{\mathrm{VLISM}}\cdot\boldsymbol{r} \sim 0$. This effectively means that some neutralized PINS with pitch angles close to 90° are preferentially detected by IBEX at 1 au from the Sun.

It has been shown that PINS outside the heliopause are sensitive to the type of turbulence present (K. Gamayunov et al. 2010, 2019; J. Giacalone & J. R. Jokipii 2015, 2020; E. J. Zirnstein et al. 2018, 2019, 2020). Here we explore turbulence using a classification system often employed in studies of the supersonic SW (G. P. Zank & W. H. Matthaeus 1992; J. W. Bieber et al. 1996), a composite of 1D slab + 2D "structure" turbulence, with ∼70%–80% of the turbulence energy in the 2D component. Slab turbulence describes 1D Alfvén wave modes that travel along the field, and 2D turbulence is referred to as structures that do not propagate. It has been shown that the slab versus 2D component varies between fast and slow SW streams (S. Dasso et al. 2005) and the plasma beta, with higher compressibility in high plasma beta regimes (G. P. Zank & W. H. Matthaeus 1992; G. P. Zank et al. 2017b; L. Matteini et al. 2020).

We note that our adopted model of turbulence includes magnetic compressions, and thus magnetic mirroring of particles near pitch angles relatively close to 90° pitch angle. In reality, it is difficult to quantify the amount of mirroring since this would involve solving for the pitch angle diffusion coefficient as a function of pitch cosine (P. Sun et al. 2016). Mirroring would be exhibited as an enhancement at pitch cosine $\mu = 0$ (F. C. Jones et al. 1978). Unfortunately, determining this is beyond the scope of the study. However, we know from prior studies (e.g., E. J. Zirnstein et al. 2023, and references therein) that in the limit of weak magnetic

turbulence (i.e., magnetic mirroring), the ribbon intensity is lower, and the peak location is farther away from the ribbon's center. Then we can infer that strong magnetic mirroring, as in the current model, would enhance the intensity of the ribbon by keeping more particles near $\boldsymbol{B}_{\rm VLISM}\cdot\boldsymbol{r} \sim 0$ for a longer period of time and move the ribbon's peak location closer to the ribbon center. If the pitch angle scattering mean free path is small enough, it can also trap particles for longer near $B_{\rm VLISM}\cdot r \sim 0$. We note that the ribbon model by Y. Huang et al. (2025) showed that as the scattering mean free path increased (up to 5000 au), the ribbon intensity increased; however, they did not test scattering mean free paths smaller than 500 au. It is currently unclear how small the scattering mean free path would need to be to potentially increase the ribbon intensity.

It is important to note that the "spatial retention" model (which assumes strong scattering; see N. A. Schwadron & D. J. McComas 2013) implemented by E. J. Zirnstein et al. (2023) in a 3D simulation of the heliosphere yields a significantly lower ribbon intensity than in the current study here, though the former did not solve for the turbulence spectrum and the kinetic transport of PUIs in the fluctuating field of the VLISM. However, the peak location of the ribbon is still closer to the ribbon center in the spatial retention model.

There are potential reasons that slab/2D turbulence may exist in the VLISM. Voyager 1, after measuring compressible turbulence within the first 10 au after crossing the heliopause, saw a conversion to almost entirely incompressible turbulence. According to G. P. Zank et al. (2017b, 2019), compressible fast magnetosonic waves transmitted across the heliopause create compressible turbulence that then soon experiences mode conversion to incompressible turbulence in the low-beta VLISM plasma. Note that our modeled field is assumed to be static in the plasma frame and does not affect the plasma fluid itself. In principle, one would therefore expect a corresponding turbulent velocity field and turbulent density fluctuations in the model (as described in G. P. Zank et al. 2017a), but only the magnetic field acts to scatter the PUIs, and the effects of turbulent velocities and densities would have a vanishingly small effect on PUI creation and loss in the VLISM.

L.-L. Zhao et al. (2020) found that the ~10 au decay/conversion seemed consistent with the observations. It was also shown that Voyager 2 observed a mode conversion within ~10 au of the heliopause similar to Voyager 1 (L. F. Burlaga et al. 2022). The continuous injection of compressible waves into the VLISM can continue to generate slab/2D wave modes in the ribbon ENA source distribution. Here, we simulate slab +2D turbulence, with different fractions of power in the slab and 2D components, and analyze the results in the context of IBEX observations (D. J. McComas et al. 2024).

2. Methodology

2.1. Ribbon Data Description

We utilize IBEX-Hi ENA observations from 2009 to 2011, where the ribbon has been separated from the globally distributed flux (L. J. Beesley et al. 2023) using flux maps processed by the IBEX Science Operations Center (D. J. McComas et al. 2024). Examples of maps at the electrostatic analyzer (ESA) step 3 (central energy of 1.11 keV) are shown in Figure 1 for the year 2009. There are five levels of ribbon-separated maps called: the "median," "upper," and "lower" limits, and the upper +1σ and

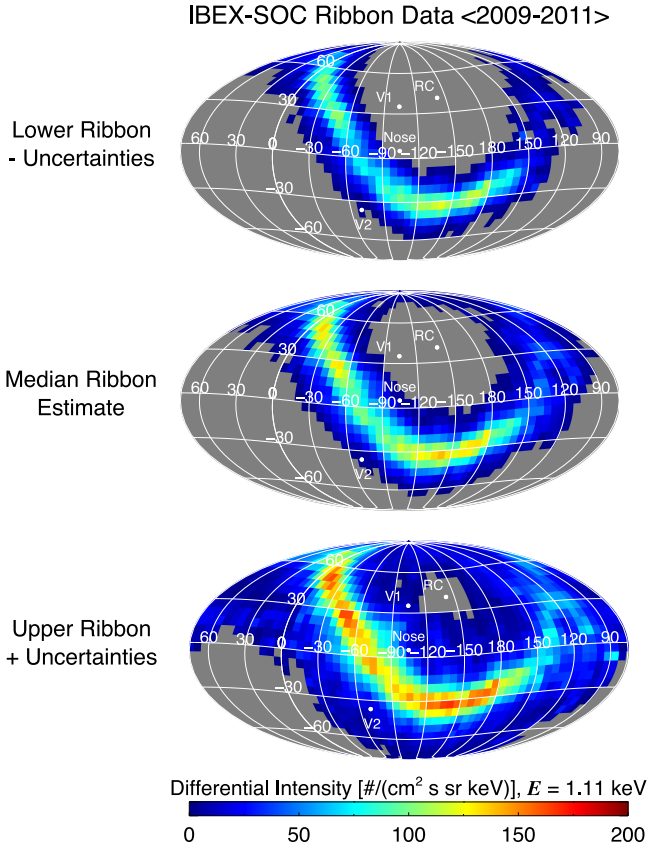

Figure 1. IBEX ribbon-only maps measured at ESA 3 (central energy 1.11 keV). The data are Compton–Getting and survival-probability corrected yearly maps weight averaged over 2009–2011.

lower −1σ ranges of uncertainty. As explained by D. J. McComas et al. (2024), the median maps are calculated from three different variations of the separation procedure, each repeated 28 times with slightly different ribbon masking assumptions. The weighted average of each set of 28, based on the goodness of separation metrics used by L. J. Beesley et al. (2023), is then calculated. Finally, with three weighted average maps, each pixelwise median is calculated to generate the median maps. The upper- and lower-limit maps are calculated from the pixelwise minimum and maximum values of the original $28 \times 3 = 84$ maps. Finally, adding and subtracting the statistical uncertainties of the upper and lower limit maps, respectively, provides the widest range possible for the ribbon fluxes, which are intended to be conservative estimates of the ribbon separation extremes. Following D. J. McComas et al. (2024), we interpret this to be the range in which a model can be considered consistent with the observations.

2.2. Ribbon Model Description

In this study, we simulate composite slab/2D turbulence with different fractions between the slab and 2D components. In the following section, we describe the setup of synthetic turbulence and how it is implemented in our ribbon ENA model.

2.2.1. Slab/2D Turbulence

We follow the methodology from J. Giacalone & J. R. Jokipii (1999) and E. J. Zirnstein et al. (2020). We compute a large number of wave modes that have random polarizations, phases, and wavevector directions. These waves are then superimposed

on our global magnetohydrodynamic (MHD) magnetic field ($\boldsymbol{B}_{\rm MHD}$) outside the heliopause. The total field is given as $\boldsymbol{B} = \boldsymbol{B}_{\rm MHD} + \delta\boldsymbol{B}$, where $\delta\boldsymbol{B}$ is the turbulent component (J. Giacalone & J. R. Jokipii 1999),

$$\delta\boldsymbol{B}(x, y, z) = \sum_{n=1}^{N} A(k_n)\,\hat{\boldsymbol{\xi}}_n \exp\left(ik_n z'_n + i\beta_n\right), \tag{1}$$

$$\hat{\boldsymbol{\xi}}_n = \cos\alpha_n \boldsymbol{x}'_n + i\sin\alpha_n \boldsymbol{y}'_n, \tag{2}$$

$$\begin{pmatrix} x' \\ y' \\ z' \end{pmatrix} = \begin{pmatrix} \cos\theta_n\cos\varphi_n & \cos\theta_n\sin\varphi_n & -\sin\theta_n \\ -\sin\varphi_n & \cos\varphi_n & 0 \\ \sin\theta_n\cos\varphi_n & \sin\theta_n\sin\varphi_n & \cos\theta_n \end{pmatrix} \begin{pmatrix} x \\ y \\ z \end{pmatrix}, \tag{3}$$

$$A^2(k_n) = 2\sigma^2 G(k_n) \Big/ \left[\sum_{n=1}^{N} G(k_n)\right] \tag{4}$$

$$G(k_n) = \frac{C_n}{1 + (k_n L_{\rm c})^{\gamma}}. \tag{5}$$

The total number of wave modes, N, is set to ~90 wave modes per decade of wavenumber (960 wave modes in total), with wavenumber $k_{\rm n}$, polarization α_n, phase β_n, wavevector direction angles θ_n and φ_n, and correlation length $L_{\rm c}$. The wave amplitude is defined by a Kolmogorov spectrum, with wave variance σ^2, and spectral index γ. The variables C_n and γ depend on the dimensionality of the turbulence. The turbulence wave variance is constrained by Voyager 1 observations (L. F. Burlaga et al. 2018), such that $\sigma^2 = 0.0015$ nT^2 and the correlation length $L_{\rm c}$ is set to be consistent with a wavelength of 50 au, i.e., $L_{\rm c} = 50/(2\pi)$ (G. P. Zank et al. 2019; E. J. Zirnstein et al. 2020; S. Xu & H. Li 2022). The maximum wavelength of integration is 150 au, and the minimum wavelength is half of a PINS's gyroradius, assuming its speed is 400 km s^{-1} in a 0.4 nT field. The matrix conversion from primed to unprimed coordinates ensures that the wave magnetic field components for a particular wavevector are perpendicular to the propagation direction of the wave.

For our purposes, Equations (1)–(5) are simplified such that the turbulent field is a composite of two components, $\delta\boldsymbol{B}(x, y, z) = \delta\boldsymbol{B}_{\rm 1D}(z) + \delta\boldsymbol{B}_{\rm 2D}(x, y)$, where the mean field ($+z$) is initially defined along the pristine ISMF direction (E. J. Zirnstein et al. 2016), i.e., the interstellar magnetic field just beyond the influence of the heliosphere. For slab turbulence, $\theta_n = 0$, $C_n = \Delta k_n$, and $\gamma = 5/3$. For 2D turbulence, $\theta_n = \pi/2$, $\alpha_n = \pi/2$, $C_n = 2\pi k_n \Delta k_n$, and $\gamma = 8/3$ (J. Giacalone & J. R. Jokipii, 1999). This turbulence model generates magnetic compressions through both slab and 2D components. The total magnetic field magnitude is given by

$$|\boldsymbol{B}| = \sqrt{B_{\rm MHD}^2 + \delta\boldsymbol{B}_{\rm 1D}\cdot\delta\boldsymbol{B}_{\rm 1D} + \delta\boldsymbol{B}_{\rm 2D}\cdot\delta\boldsymbol{B}_{\rm 2D} + 2\delta\boldsymbol{B}_{\rm 1D}\cdot\delta\boldsymbol{B}_{\rm 2D}}. \tag{6}$$

Even the inclusion of just one turbulent component (for example, $\delta B_{\rm 1D}$) yields magnetic field magnitude variations because $\delta B_{\rm 1D}$ is a function of z, and $\delta B_{\rm 1D}^2$ is the multiplication of two separate sums over all wavevectors. Thus, $|B|$ is not constant. Note that the same argument can be applied to $\delta B_{\rm 2D}$. In fact, it is difficult to create a field that varies in three dimensions while having $|\boldsymbol{B}|$ = constant (D. A. Roberts 2012).

The slab and 2D modes in our model are defined in adjacent numbers from $n = 1$ to $N_{\rm m}$, i.e., wave mode 1 is slab, wave mode 2 is 2D, wave mode 3 is slab, etc. This ensures that we have an equal number of slab and 2D waves at all scales. Then we divide the total turbulence power into the two components' wave variances, σ^2, in different fraction combinations. We note that because the wave modes are iterated between slab and 2D, the spacing between wave modes in k-space becomes $\Delta k_n = k_{n+1} - k_{n-1}$.

Equations (1)–(5) are calculated assuming the global mean field is toward $+z$. However, we want to have the global mean field aligned with the local MHD magnetic field, which changes direction as a function of position (x, y, z) as it drapes around the heliosphere. To maintain a divergence-free magnetic field, we cannot rotate each wavevector at every position (x, y, z) at each particle step, which would break the divergence-free condition. Instead, for each particle, we rotate the slab $+z$ axis to be parallel to the local MHD field of the particle's location only once, and keep it constant for the lifetime of the particle, which we define as the e-folding, charge exchange lifetime $\tau_{ex} = 1/(n_H \sigma_{ex} v_p)$, where n_H is the local interstellar neutral H density, σ_{ex} is the charge exchange cross section, and v_p is the proton's speed. For the next particle, we reorient the slab $+z$ axis to align with the new local MHD field where the next particle is, and repeat accordingly.

The trajectories of the parent PUIs gyrating around the total field $\boldsymbol{B}$ are solved by numerically integrating the Lorentz force equation using the Bulirsch–Stoer method (W. H. Press et al. 2002), in the nonrelativistic limit,

$$\frac{d\boldsymbol{v}_{\rm p}}{dt} = \frac{q}{m_{\rm p}c}\boldsymbol{v}_{\rm p} \times \boldsymbol{B}, \tag{7}$$

where $\boldsymbol{v}_{\rm p}$ is the proton's velocity, q is its charge, $m_{\rm p}$ is the proton mass, and c is the speed of light, presented in centimeter-gram-second units. Equations (1)–(5) and (7) are solved at every substep of the integration. Note that we do not include an $\boldsymbol{E} \times \boldsymbol{B}$ drift effect in Equation (7), created by the advection of PUIs with the bulk VLISM plasma flow. We do not expect the energy to change significantly due to this effect, but it may have a slight effect on the ribbon source region (E. J. Zirnstein et al. 2018; Y. Huang et al. 2025).

We note that K. H. Lee & L. C. Lee (2020) showed there is an enhancement in magnetic field turbulence at length scales mk = $10^{-8.8}$–$10^{-8.2}$ and that the magnetic power spectral slope becomes slightly flatter for m$k > 10^{-8.2}$ (or $1/k < 10^{8.2}$ m, where k is a wavenumber and m is the unit meter), with a slope close to -1 instead of the Kolmogorov scaling of $-5/3$. We find that in a 0.5 nT magnetic field, typical of the VLISM near the heliopause as measured by the Voyagers, the gyroradius of a 1.11 keV proton is approximately 10^7 m. Therefore, the gyroradius of a 1.11 keV proton in our model falls in the range where the observed magnetic power spectrum deviates from a Kolmogorov spectrum. We discuss the implications of this in Section 4.

Our analytical model does not formally contain wave–wave interactions and the nonlinear cascade of MHD turbulence, but since we use a power law Kolmogorov-like (we could also have used a flatter Iroshnikov–Kraichnan power-law scaling), there is an implicit assumption that resonant self-similar interactions of fluctuations result in a nonlinear cascade of magnetic and kinetic energy from large to small scales. This is consistent with our assumption of static turbulence. Numerical modeling of turbulence, e.g., via large-scale driving that produces an energy cascade (P. Dmitruk & W. H. Matthaeus 2009; A. Beresnyak 2019; Z. Gan et al. 2022), can naturally

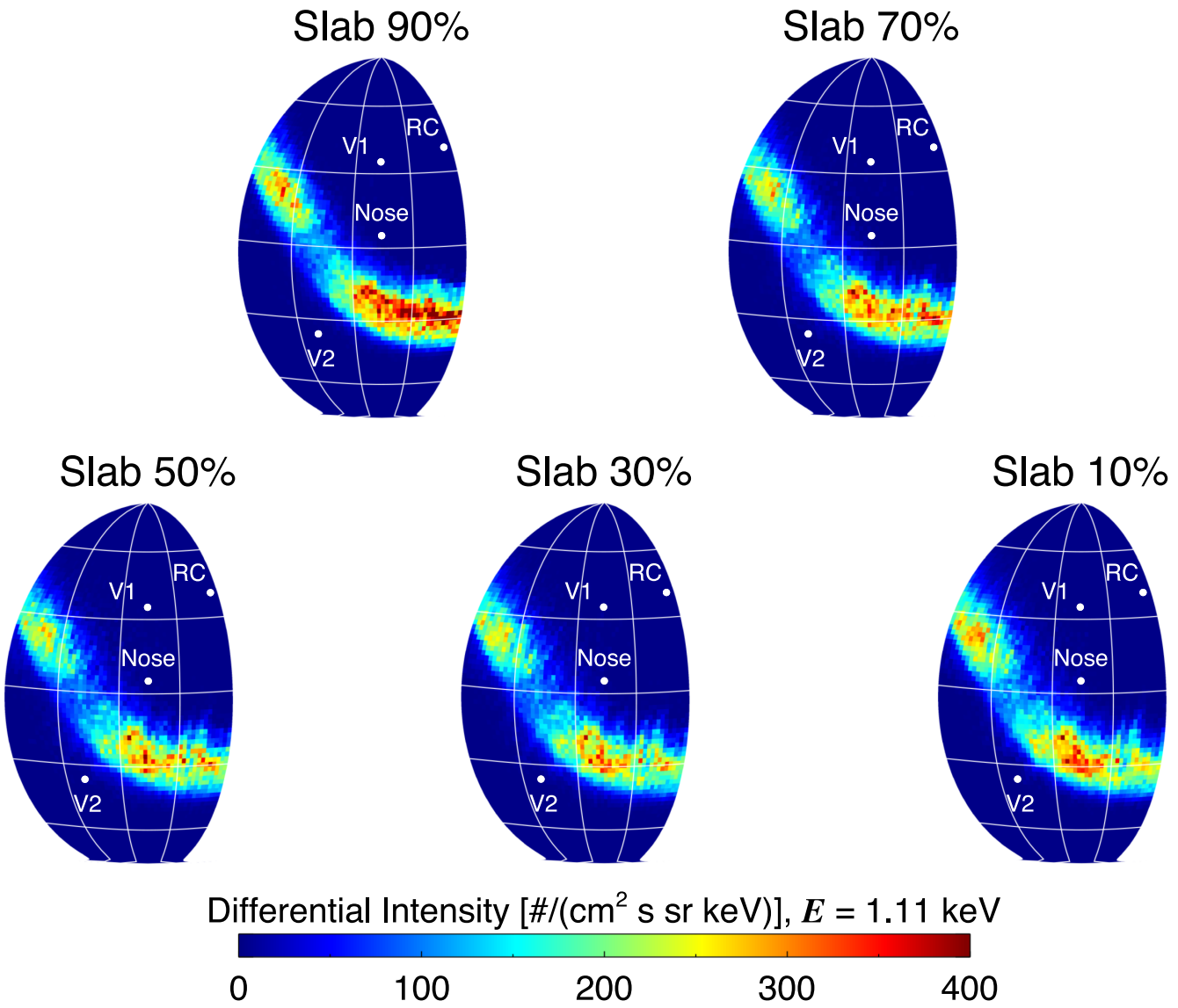

Figure 2. Partial sky maps of the modeled ribbon, with five ratios of slab turbulence: slab-90%/2D-10%, slab-70%/2D-30%, slab-50%/2D-50%, slab-30%/2D-70%, and slab-10%/2D-90% turbulence. Note the color scale is different than Figure 1.

produce a Kolmogorov energy spectrum. We simply assume that the energy spectrum is Kolmogorov, which is a frequently made and reasonable assumption. Some advantages of our adopted model over those with large-scale driving in direct numerical simulations are that numerical turbulence simulations usually only resolve a limited range of scales (i.e., a few decades) due to the finite resolution of the model. Further, they generally solve for a steady-state configuration with uniform background geometry. By employing an analytic model, we can extend the range of scales as far as needed in the VLISM and can include effects such as a nonuniform background field, which is an important property of the interstellar magnetic field as it drapes around the heliosphere.

3. Results and Discussion

3.1. Model Ribbon Partial Sky Maps

Figure 2 shows the model results for five different slab+2D turbulence cases. First, note that we do not calculate entire sky maps of the ribbon due to computational limitations. The SW neutral source distribution that produces these modeled ribbon ENAs is extracted from the yearly neutral source data created by E. J. Zirnstein et al. (2023) from interplanetary scintillation (IPS)-based SW speed and OMNI observations of the SW speed and density. We take the SW neutral source fluxes as a function of time and average over 2004 through 2008, which approximately overlaps IBEX observations from 2009 through 2011, given a total time delay of ∼3–5 yr depending on the direction in the sky. Assuming a ribbon source at 150 au, particle speed of 460 km s^{-1} (the speed of a 1.11 keV proton), and neutral H density in the ribbon source region of 0.2 cm^{-3}, we get a total time delay of ∼4 yr. We add and subtract 1 yr for potential uncertainties in the calculation, leading us to average over the years 2004 through 2008. If we had more computational resources, we could perform a more thorough, time-dependent calculation of the ribbon, following, e.g., E. J. Zirnstein et al. (2023).

As can be seen in Figure 2, the highest slab percentage of turbulence power roughly yields the highest ribbon intensity because this type of turbulence allows for more PINS with

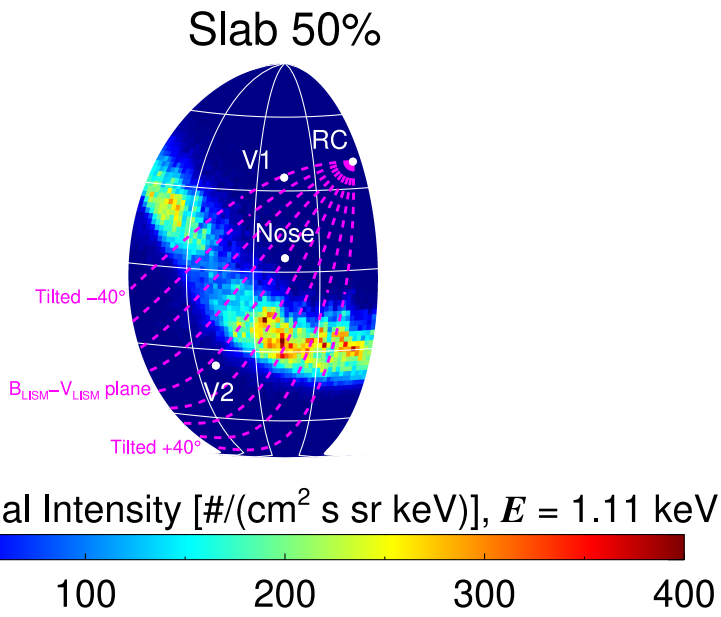

Figure 3. Partial sky map of the modeled ribbon case for slab-50%/2D-50% with nine great circles drawn across the ribbon starting from the ribbon center (RC). We take cross sections of the ribbon along these great circles to compare the intensities and peak locations between the models and data.

pitch angles close to 90°, generating ENAs with velocities coming back toward Earth from IBEX look directions near $\boldsymbol{B}_{\rm VLISM}\cdot\boldsymbol{r} = 0$. Also, although it is not clear from Figure 2, the angular distance from the ribbon center is different depending on the slab percentage used in the model.

We do a more in-depth analysis of our model by taking nine cross sectional cuts across the ribbon for all models and the data. The nine cuts, or great circles, are shown in Figure 3. We first choose the $\boldsymbol{B}_{\rm VLISM}$–$\boldsymbol{V}_{\rm VLISM}$ plane, where we use the observed ribbon center (M. A. Dayeh et al. 2019) instead of the pristine $\boldsymbol{B}_{\rm VLISM}$ (E. J. Zirnstein et al. 2016), mostly for convenience, so readers can see the angular distance of the ribbon peak from its center, i.e., the ribbon "radius" (H. O. Funsten et al. 2009, 2013; S. A. Fuselier et al. 2009; D. J. McComas et al. 2009b; M. A. Dayeh et al. 2019). Note that the ribbon center lies on the $\boldsymbol{B}_{\rm VLISM}$–$\boldsymbol{V}_{\rm VLISM}$ plane (E. J. Zirnstein et al. 2016). We then take more great circles spread 10° apart on either side, as shown in Figure 3, making nine in total.

3.2. Cross Sectional Cuts of the Ribbon Model and Data

Figure 4 shows a panel for each cut across the ribbon. We take 3° steps along the planes (Figure 3) and average the nearest 9 pixels to produce the curves shown in Figure 4. The solid black curve is the data's median ribbon estimate ("M"), the edges of the dark gray contours indicate the upper ("U") and lower ("L") ribbon estimates, and the edges of the light gray contours indicate the upper and lower ribbon estimates plus and minus their statistical uncertainties, respectively ("U $+\sigma$" and "L$-\sigma$"). These contours represent the boundaries within which the ribbon is very likely to exist (D. J. McComas et al. 2024). The colored curves are the model results. Upon first inspection, one can see that, in general, most of the simulated ribbon intensities are too high compared to the observations. This is true for at least six out of nine cross sections: the three exceptions are the great circles tilted by $-10°$, $-20°$, and $-30°$ from the $\boldsymbol{B}_{\rm VLISM}$–$\boldsymbol{V}_{\rm VLISM}$ plane. In these three cuts, all models are reasonably close to the observed level of intensities (within the gray contours). However, note that, in all panels, the modeled ribbon peaks are slightly different for each turbulence case we consider. This will be analyzed later in Section 3.

Another interesting observation is that most of the models (except slab-90%) in the $\boldsymbol{B}_{\rm VLISM}$–$\boldsymbol{V}_{\rm VLISM}$ plane cross section (Figure 4(c)) have ribbon peaks that are shifted away from the ribbon center the most, by approximately one IBEX pixel (6°). Moreover, most of the modeled ribbon intensities are higher than the observed intensities. Although we do not know why this discrepancy occurs most noticeably along the $\boldsymbol{B}_{\rm VLISM}$–$\boldsymbol{V}_{\rm VLISM}$ plane cross sectional cut, there are several possible reasons that could cause this behavior in general. First, it may be related to the fact that we are only able to simulate the ribbon at exactly 1.11 keV, due to computational limitations, rather than integrating over the ESA 3 energy response function (centered on 1.11 keV). Another possible reason is the realization of turbulence used in our models. As E. J. Zirnstein et al. (2020) showed, different turbulence realizations may change the position of parts of the ribbon. However, to help mitigate this issue, we simulate the ribbon with more wave modes, ∼90 per decade, instead of ∼45 per decade as was done by E. J. Zirnstein et al. (2020). In our analysis, we found that ∼90 modes per decade and above produce similar results. A third potential reason is that some of the turbulence may still be compressible, which at long wavelengths will look like Alfvén waves and introduce different PUI scattering behavior (introducing $\delta B_{\parallel}$ in Equation (7)) than we currently solve for. In fact, a recent analysis by S. Xu & H. Li (2023) showed that compressible fast modes in MHD turbulence act as magnetic mirrors to particles in the VLISM, which can produce mirroring and pitch angle scattering effects that allow the accumulation of PUIs near $\boldsymbol{B}_{\rm VLISM}\cdot\boldsymbol{r} \sim 0$. In a future study, we plan to better understand these effects.

We analyze the peak locations of the model and data by normalizing the intensities to their peaks, and identify where the peaks' locations are, shown as vertical lines in Figure 5. Here, it is easier to see how well the peak locations compare to

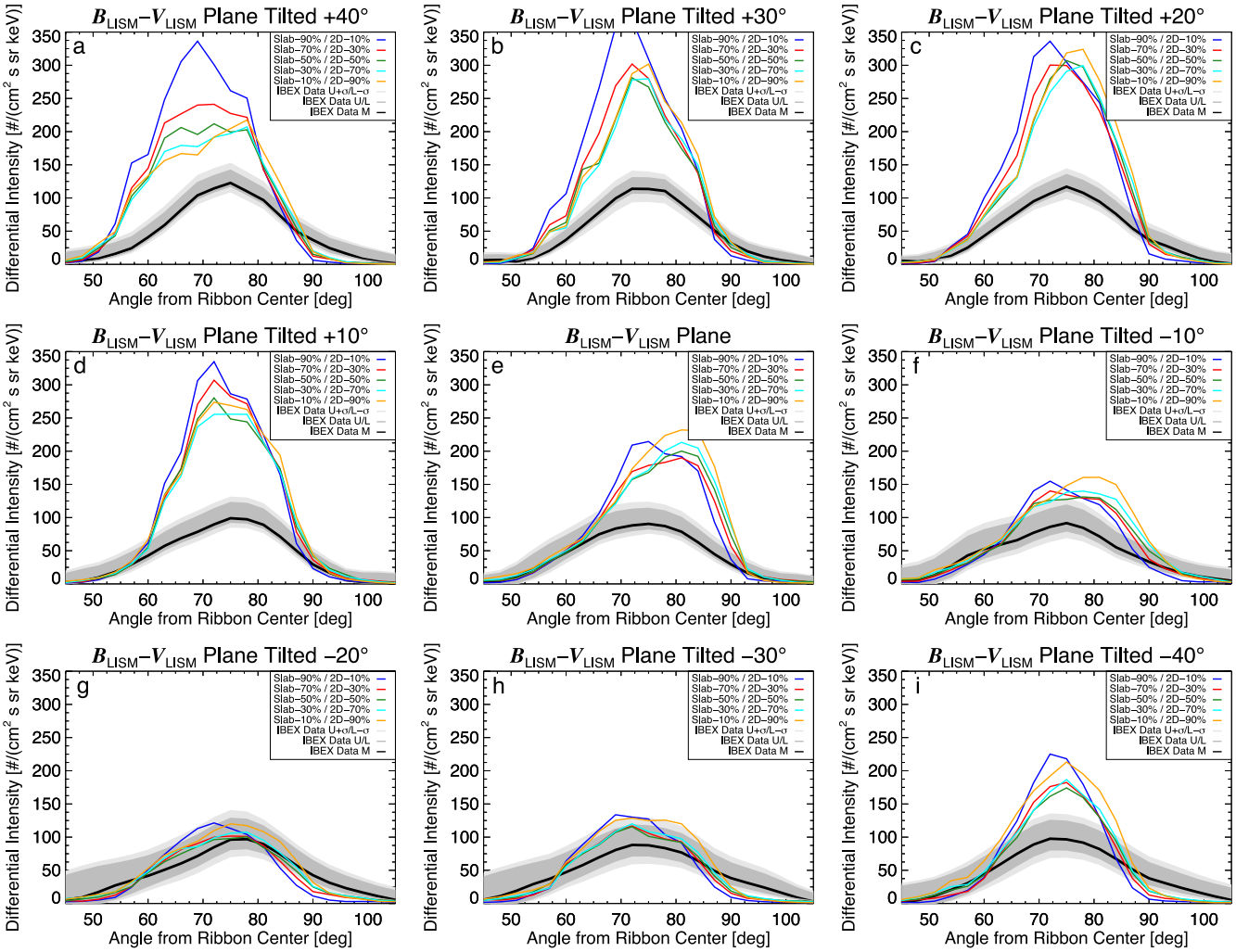

Figure 4. Comparison of nine cross sections across the ribbon between the models (colored curves) and the data (black curve and dark/light gray contours).

the observations, and from one model to another. The modeled and observed ribbon peak locations are identified by the vertical lines, which have different heights and colors to differentiate them. For most of the results in Figure 5, the model results (vertical, colored lines) compare well to the data (vertical, black line). For our assumed 1σ uncertainty of 3°, most of the modeled ribbon peaks lie within 1σ of the data. There are some cases where there are outliers (Figures 5(a), (e), (f), and (g)). We calculate a rough estimation of the most likely slab fraction model based on the peaks' comparisons. First, we designate any peak location >3° from the observed ribbon peak as outliers and do not include them in the calculation. Then, we calculate the average slab percentage of the remaining peak locations in all panels together, finding an average of slab-50%. The standard deviation is 28% and the standard error is 5% (Table 1).

Obtaining an average of 50% slab turbulence does not necessarily mean it is the best-fit model. However, there are results in four panels (Figures 5(a), (e), (f), and (g)) where there is at least one outlier eliminated from the calculation of the average (see also Table 1). Counting the number of cases in the average, there is one less slab-90% case and one less slab-10% case, making the average symmetric around the slab-50% case. While the standard deviation is large, essentially only ruling out the slab-90% and slab-10% cases, the standard error is small, ruling out all but the slab-50% case. Therefore, we interpret the results as follows: the slab-50% case is the preferred average of the spatially dependent, slab/2D turbulence fraction in the VLISM, but not necessarily the only choice, primarily due to the high intensities of the model. On the other hand, the intensities of the slab-50% ribbon (see Figure 4) are somewhat closer to the data than the other model cases.

3.3. Changing the Neutral Solar Wind Source

One main caveat to our analysis is that our model is a steady-state calculation that uses time-averaged, IPS-derived SW speeds to create the neutral SW source of the ribbon. Instead of simulating the ribbon as a function of time (E. J. Zirnstein et al. 2023), which is computationally expensive for the type of model presented in this paper, we averaged the IPS-derived results over 2004 through 2008 to produce our neutral SW source. Our choice of 2004 through 2008 is based on comparing to IBEX ENA data taken in 2009 through 2011 (i.e., a time delay of ∼3–5 yr). However, as shown in Figure 4, the model intensities, particularly at negative latitudes (a positive angle tilt from the *B*–*V* plane), are much higher than the observations. We suggest that this may at least be partially due to our choice to average over 2004

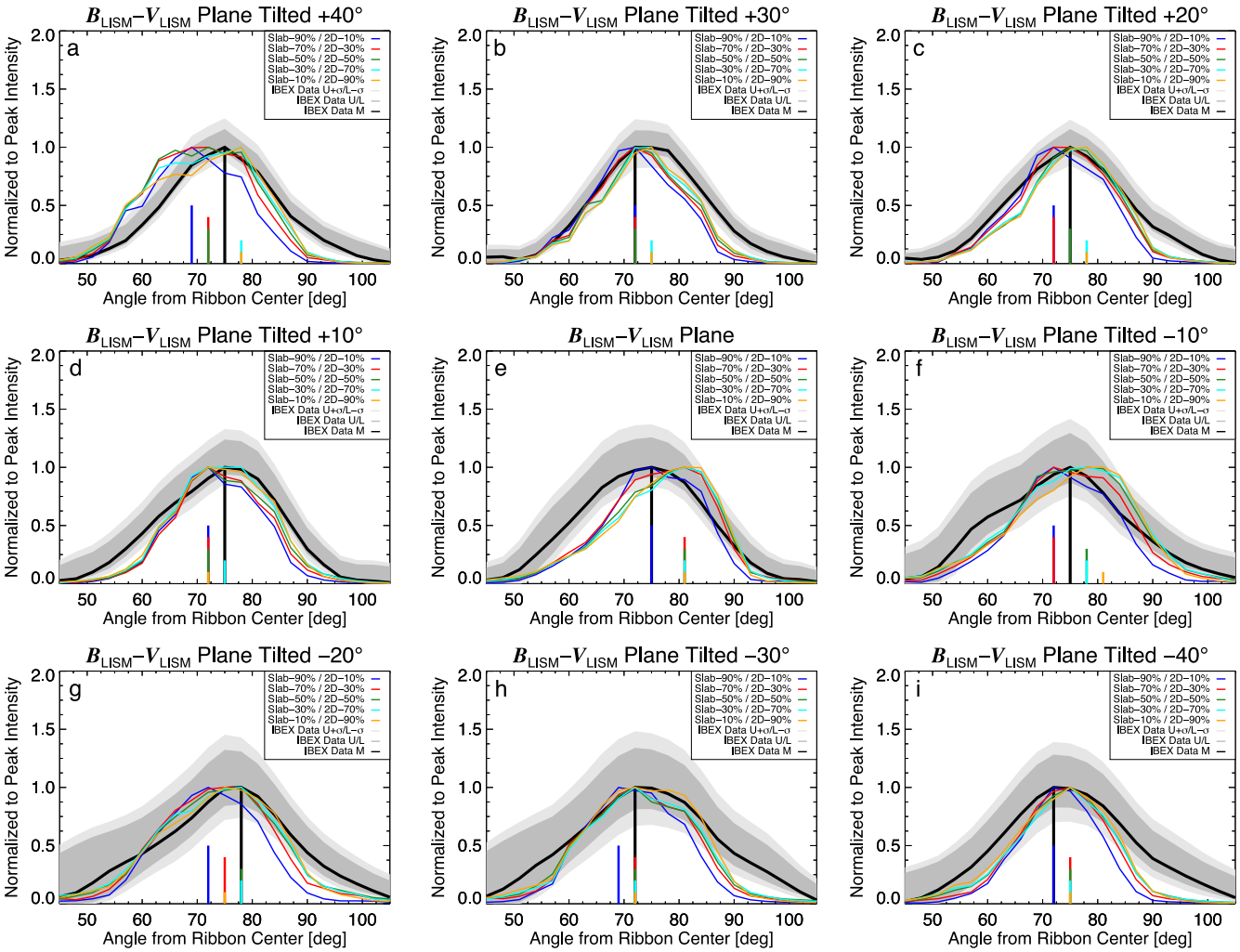

Figure 5. Similar to Figure 4, except the intensities are normalized to their peak, and the peak intensities' locations are shown as vertical lines. The height of the vertical lines is only meant to help differentiate results that have the same peak location. The resolution of the models and data is 3°. Results suggest an average slab percentage of 50% ± 28% (standard deviation) and ±5% (standard error).

Table 1
Comparison of the Models to the Data as Shown in Figure 5

Tilt from B_{LISM}–V_{LISM} Plane (deg)	Within 1σ of Data Peak (Slab%)
+40	10, 30, 50, 70
+30	All
+20	All
+10	All
0	90
−10	30, 50, 70, 90
−20	10, 30, 50, 70
−30	All
−40	All
Number of values	38
Mean (%)	50
Standard Deviation (%)	28
Standard Error (%)	5

through 2008 for the neutral SW source, i.e., the modeled ribbon may be sensitive to the time period we average over.

Here we consider the appearance of the modeled ribbon (i.e., the slab-50% case) if we slightly adjust the time period over which we average the IPS-derived SW speeds. Figure 6 shows the modeled ribbon for the original period (<2004–2008>), along with <2005–2007> and <2006–2008>. As one can see, using slightly different time periods can significantly change the intensity of the ribbon. The intensity decreases mostly in the northern hemisphere for both <2005–2007> and <2006–2008>, but the greatest change, which also noticeably decreases the intensity in the southern hemisphere, is the case where we averaged over 2006 through 2008. These years better reflect solar minimum (open polar coronal holes) conditions, which produce higher intensities at energies higher than ∼1 keV, thus decreasing the intensity of ∼1 keV ribbon ENAs. It appears, though, that including the year 2004 is the main reason for producing the higher intensities. The simulations in later years, particularly <2006–2008>, also decrease the intensity near the ecliptic plane, making the comparison with the data worse. Therefore, one must carefully choose the time period for comparing to IBEX data and consider the importance of performing time-dependent simulations if possible.

4. Conclusions

In this study, we have analyzed the effects of slab/2D turbulence in the VLISM where the ribbon is formed. We also

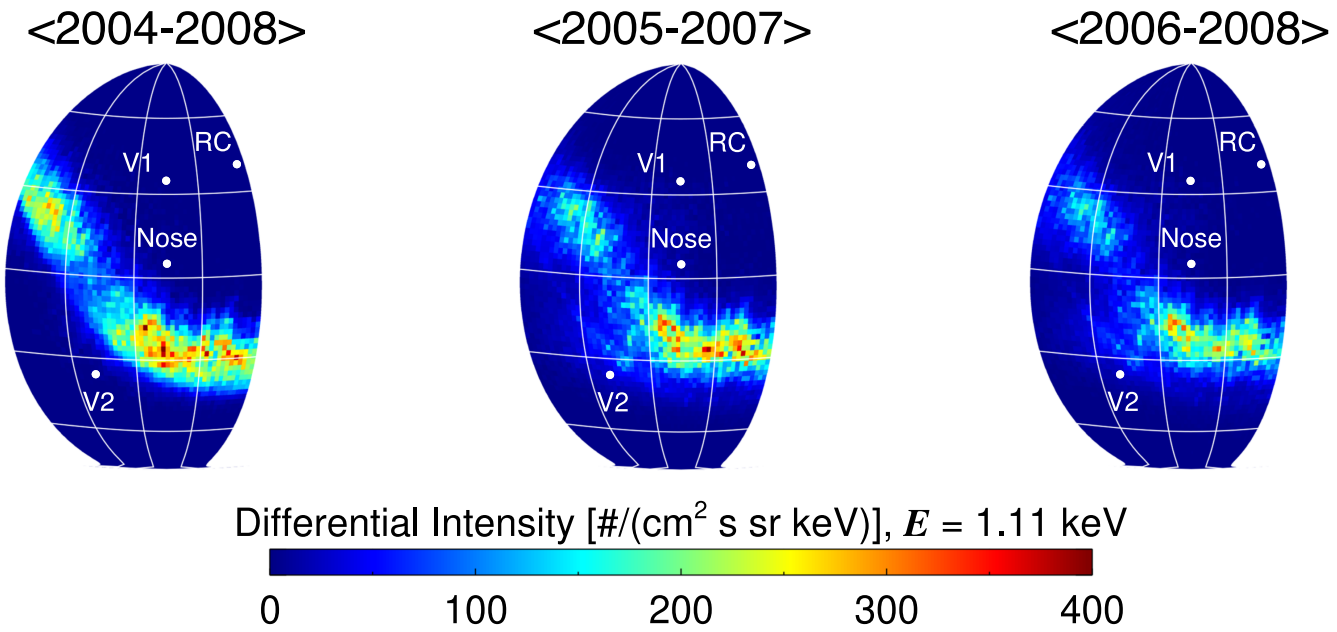

Figure 6. Simulated ribbon maps for the slab-50% case, where the neutral SW source is averaged over (left) 2004 through 2008, (middle) 2005 through 2007, and (right) 2006 through 2008.

examined what percentage of the heliosphere-originating turbulence is slab-like. This is done by simulating the ribbon in several different turbulence scenarios (different fractions of slab to 2D of the total turbulence power) and comparing the intensity and peak location of the ribbon cross section to IBEX ribbon-separated data (D. J. McComas et al. 2024). We first find that the ribbon model intensities are, for the most part, higher than the data, except near the ecliptic plane. Thus, we cannot discern which slab fraction is best based on the intensities alone.

We then compared the peak locations of the ribbon between the models and data by normalizing the fluxes of each model and the data to their own ribbon peaks and finding which of the models lie within 3° of the data (see Figure 5 and Table 1). We find that an estimated/preferred result of the slab+2D turbulence spectrum is slab-50%/2D-50%, with 28% standard deviation and 5% standard error. If we were to take slab-50% as the nominal case, this is consistent with slab/2D ratios predicted by G. P. Zank & W. H. Matthaeus (1991) and G. P. Zank et al. (2017a), who show that in the low plasma beta limit, the slab/2D fraction would be closer to ∼20/80 in a "pristine" plasma. Except, now with the injection of compressible modes from the heliosphere, some of which undergo mode conversion (G. P. Zank et al. 2019), this would add to the slab fraction as our analysis suggests. However, we do not claim this result applies everywhere in the sky, but it is an estimated result to use before we can better understand the spatial dependence of slab/2D turbulence in the VLISM. The slab/2D fraction can depend on the ability of Alfvén waves to travel through the VLISM away from the heliopause, determined by the relative angles between the VLISM plasma flow and ISMF directions.

As mentioned in Section 2.2.1, K. H. Lee & L. C. Lee (2020) show that the magnetic power spectral slope inferred from Voyager observations becomes slightly flatter for m$k > 10^{-8.2}$ (or $1/k < 10^{8.2}$ m), with a slope close to −1 instead of the Kolmogorov scaling of −5/3. However, F. Fraternale et al. (2019) point out that the spectral flattening occurs primarily in the Voyagers' noise band and is therefore likely due to noise. Our model assumes a Kolmogorov spectral slope over all scales, normalized to match data given by L. F. Burlaga et al. (2018). Because the gyroradius of a 1.11 keV proton lies within the range where the observed spectral slope is −1, it is possible that the flattening of the magnetic spectrum to a ∼−1 spectral slope would affect our results because this would imply that the amplitude of turbulence power is higher than assumed in our model, potentially leading to strong mirroring and pitch angle scattering. However, besides the possibility that the flattening of the magnetic spectrum is due to instrumental noise, there is a potential inconsistency with the density fluctuation spectrum over the m$k > 10^{-8.2}$ interval, which mostly follows a $k^{-5/3}$ Kolmogorov spectrum (except for the enhancement in the ∼50–10^6 m range, which does not overlap the 1.11 keV proton gyroradius scale of 10^7 m). As argued by D. Montgomery et al. (1987) and subsequently by G. P. Zank & W. H. Matthaeus (1992, 1993), the fluctuating density spectrum can be directly related to the form of the fluctuating magnetic spectrum via the so-called "pseudo-sound" relation so that one can infer a $k^{-5/3}$ magnetic power spectral density (PSD) from a corresponding $k^{-5/3}$ density PSD. Since the density spectra are more accurately measured by the Voyager Plasma Wave Subsystem in this wavenumber range, one would expect that the magnetic field PSD would track the Kolmogorov power law exhibited by the density fluctuations closely.

Several simplifications were made to the analysis to minimize the simulations' computational time, such as simulating only one energy in the IBEX-Hi ESA 3 passband (centered at 1.11 keV) and using a neutral SW source that is time-averaged from 2004 through 2008. We showed that by choosing different time periods to average over (Figure 6), the intensity can significantly decrease and better match the data. This illustrates how sensitive the ribbon model is to the time period used, and potentially the necessity for modeling the ribbon as a function of time, which may give modeled intensities that better match the data.

While we only partially mitigated the potential issues of our model simplifications, it is still insightful that IBEX observations can help constrain VLISM turbulence to the extent that is consistent with Voyager 1 observations of the total turbulence power, as well as the theory behind it. We anticipate that a deeper analysis with Interstellar Mapping and Acceleration Probe (D. J. McComas et al. 2018) observations will better constrain the spatially dependent, slab/2D turbulence in the VLISM. Also, the results may be improved in the future with more computational resources and a time-dependent neutral SW source, which is beyond the scope of this study.

Acknowledgments

This work was supported by NASA's IBEX mission (80NSSC20K0719) and IMAP mission (80GSFC19C0027). It is also partially supported by the Laboratory Directed Research and Development (LDRD) program of Los Alamos National Laboratory (LANL). E.J.Z. acknowledges partial support from the LDRD-LANL program under sponsor award No. CW 18805.

ORCID iDs

E. J. Zirnstein https://orcid.org/0000-0001-7240-0618
D. J. McComas https://orcid.org/0000-0001-6160-1158
J. Giacalone https://orcid.org/0000-0002-0850-4233
G. P. Zank https://orcid.org/0000-0002-4642-6192
F. Guo https://orcid.org/0000-0003-4315-3755
J. Heerikhuisen https://orcid.org/0000-0001-7867-3633
H. Li https://orcid.org/0000-0003-3556-6568
D. B. Reisenfeld https://orcid.org/0000-0003-1874-9450

References

Beesley, L. J., Osthus, D., Moran, K. R., et al. 2023, arXiv:2302.03089
Beresnyak, A. 2019, LRCA, 5, 2
Bieber, J. W., Wanner, W., & Matthaeus, W. H. 1996, JGR, 101, 2511
Burlaga, L. F., Florinski, V., & Ness, N. F. 2018, ApJ, 854, 20
Burlaga, L. F., Ness, N. F., Berdichevsky, D. B., et al. 2022, ApJ, 932, 59
Dasso, S., Milano, L. J., Matthaeus, W. H., & Smith, C. W. 2005, ApJL, 635, L181
Dayeh, M. A., Zirnstein, E. J., Desai, M. I., et al. 2019, ApJ, 879, 84
Dmitruk, P., & Matthaeus, W. H. 2009, PhPl, 16, 062304
Fraternale, F., Pogorelov, N. V., Richardson, J. D., & Tordella, D. 2019, ApJ, 872, 40
Funsten, H. O., Allegrini, F., Crew, G. B., et al. 2009, Sci, 326, 964
Funsten, H. O., DeMajistre, R., Frisch, P. C., et al. 2013, ApJ, 776, 30
Fuselier, S. A., Allegrini, F., Funsten, H. O., et al. 2009, Sci, 326, 962
Gamayunov, K., Zhang, M., & Rassoul, H. 2010, ApJ, 725, 2251
Gamayunov, K. V., Heerikhuisen, J., & Rassoul, H. K. 2019, ApJL, 876, L21
Gan, Z., Li, H., Fu, X., & Du, S. 2022, ApJ, 926, 222
Giacalone, J., & Jokipii, J. R. 1999, ApJ, 520, 204
Giacalone, J., & Jokipii, J. R. 2015, ApJL, 812, L9
Giacalone, J., & Jokipii, J. R. 2020, ApJL, 897, L45
Gurnett, D. A., & Kurth, W. S. 2019, NatAs, 3, 1024
Gurnett, D. A., Kurth, W. S., Burlaga, L. F., & Ness, N. F. 2013, Sci, 341, 1489
Heerikhuisen, J., Pogorelov, N. V., Zank, G. P., et al. 2010, ApJL, 708, L126
Huang, Y., Guo, F., Zirnstein, E. J., et al. 2025, ApJ, 987, 192
Jones, F. C., Birmingham, T. J., & Kaiser, T. B. 1978, PhFl, 21, 347
Lee, K. H., & Lee, L. C. 2020, ApJ, 904, 66
Matteini, L., Franci, L., Alexandrova, O., et al. 2020, FrASS, 7, 83
McComas, D. J., Alimaganbetov, M., Beesley, L. J., et al. 2024, ApJS, 270, 17
McComas, D. J., Allegrini, F., Bochsler, P., et al. 2009a, SSRv, 146, 11
McComas, D. J., Allegrini, F., Bochsler, P., et al. 2009b, Sci, 326, 959
McComas, D. J., Christian, E. R., Schwadron, N. A., et al. 2018, SSRv, 214, 116
Montgomery, D., Brown, M. R., & Matthaeus, W. H. 1987, JGR, 92, 282
Press, W. H., Teukolsky, S. A., Vetterling, W. T., & Flannery, B. P. 2002, Numerical Recipes in C: The Art of Scientific Computing (2nd ed.; Cambridge: Cambridge Univ. Press)
Roberts, D. A. 2012, PhRvL, 109, 231102
Schwadron, N. A., & McComas, D. J. 2013, ApJ, 764, 92
Sun, P., Jokipii, J. R., & Giacalone, J. 2016, ApJ, 827, 16
Xu, S., & Li, H. 2022, ApJL, 941, L19
Xu, S., & Li, H. 2023, ApJ, 957, 97
Zank, G. P., Adhikari, L., Hunana, P., et al. 2017a, ApJ, 835, 147
Zank, G. P., Du, S., & Hunana, P. 2017b, ApJ, 842, 114
Zank, G. P., & Matthaeus, W. H. 1991, PhFlA, 3, 69
Zank, G. P., & Matthaeus, W. H. 1992, JGR, 97, 17189
Zank, G. P., & Matthaeus, W. H. 1993, PhFlA, 5, 257
Zank, G. P., Nakanotani, M., & Webb, G. M. 2019, ApJ, 887, 116
Zhao, L.-L., Zank, G. P., & Burlaga, L. F. 2020, ApJ, 900, 166
Zirnstein, E. J., Giacalone, J., Kumar, R., et al. 2020, ApJ, 888, 29
Zirnstein, E. J., Heerikhuisen, J., & Dayeh, M. A. 2018, ApJ, 855, 30
Zirnstein, E. J., Heerikhuisen, J., Funsten, H. O., et al. 2016, ApJL, 818, L18
Zirnstein, E. J., Heerikhuisen, J., & McComas, D. J. 2015, ApJL, 804, L22
Zirnstein, E. J., McComas, D. J., Schwadron, N. A., et al. 2019, ApJ, 876, 92
Zirnstein, E. J., Swaczyna, P., Dayeh, M. A., & Heerikhuisen, J. 2023, ApJ, 949, 45